ACS Macro Letters

Letter

pubs.acs.org/macroletters

Imaging the Molecular Structure of Polyethylene Blends with Broadband Coherent Raman Microscopy

Young Jong Lee,*[,†] Chad R. Snyder,[†] Aaron M. Forster,[‡] Marcus T. Cicerone,[†] and Wen-li Wu*[,†]

[†]Polymers Division, Material Measurement Laboratory, National Institute of Standards and Technology, Gaithersburg, Maryland 20899, United States

[‡]Materials and Structural Systems Division, Engineering Laboratory, National Institute of Standards and Technology, Gaithersburg, Maryland 20899, United States

Supporting Information

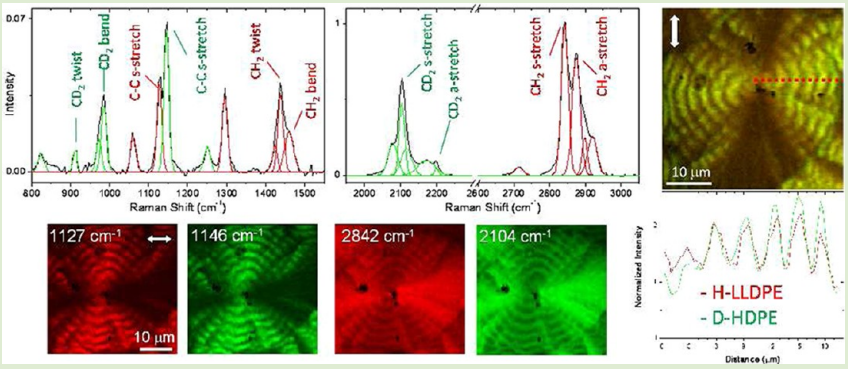

ABSTRACT: Polyethylene (PE) has been widely used in a myriad of consumer products and critical infrastructure products such as underground gas and water pipes. These products are often made of blends of multiple types of PE with different molecular architectures. Although the long-term performance of these products is largely dictated by their local molecular structure, it has been studied mostly by indirect and bulk-averaging methods such as calorimetry and neutron scattering due to lack of chemical contrast for conventional imaging techniques. We demonstrate that broadband coherent anti-Stokes Raman scattering (CARS) microscopy can acquire images of the chemical composition and molecular orientation of a miscible semicrystalline PE blend with two different molecular architectures. We discuss the detailed crystal structure observed at different length scales and new insights it provides into polymer crystal morphology.

Polyolefins, including polyethylene and polypropylene, account for the largest volume of polymer materials produced in the world. They are a ubiquitous class of materials with a broad range of applications such as diapers, milk bottles, geomembranes for groundwater protection, furniture, automotive parts, and pipes. Blends of polyethylenes (PE) with different molecular architectures and molecular masses are increasingly used for improving reliability, performance, and service life. For example, PE piping is currently being used to replace the aged water mains in our cities, the delayed maintenance of which has resulted in over 240 000 pipe breaks per year, leaks wasting 1.7 trillion gallons of water, and costs to taxpayers of $2.6 billion per year.[1] The prevailing PE candidates are blends of branched and linear materials with a predicted service life up to 100 years. The local failure in these blends is related to the microscopic structure, such as crystallization and phase separation on the micrometer and submicrometer scales; however, conventional measurements based on bulk properties cannot provide quantitative and morphological information on the local molecular structure. Despite high spatial resolving power, atomic force microscopy methods can only observe physical features at the surface and are extremely limited in providing information on molecular composition or orientation. General electron or optical microscopy techniques are also limited by the lack of chemical contrast between the organic components in these blend systems.

The semicrystalline structure of PE homopolymers studied with conventional imaging and scattering methods is briefly summarized as follows. On a molecular length scale, a semicrystalline lamella consists of well-packed polymer chains with the chain axis (the crystal *c*-axis) nearly normal to the crystal lamella, as demonstrated by X-ray scattering.[2,3] A fraction of chains located at the interlamellar regions are amorphous without preferential orientation. In a spherulite (Figure 1a–c) such lamellae grow in the form of stacked ribbons from the center radially along the crystal *b*-axis.[4] As the multiple branches of the lamellar stacks grow, they can sometimes twist coherently with neighboring stacks, resulting

Received: October 15, 2012
Accepted: November 2, 2012
Published: November 8, 2012

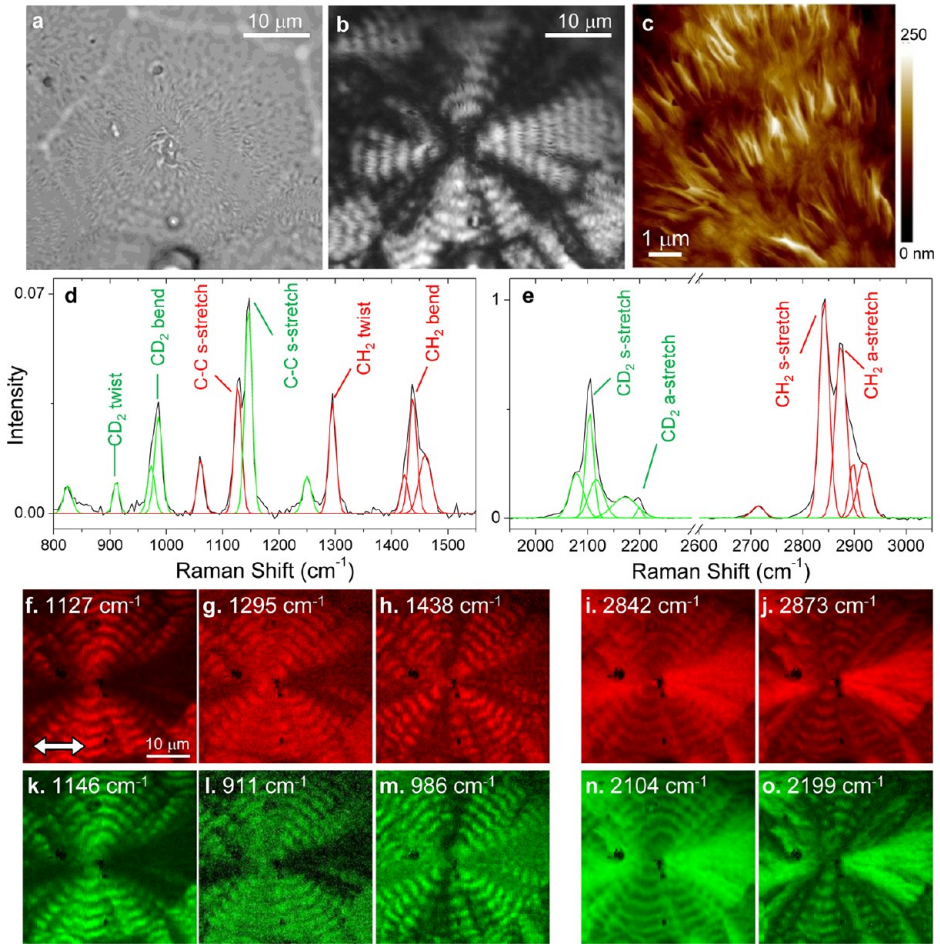

Figure 1. CARS spectrum and mode-specific images of spherulitic structures formed in the polyethylene (PE) blend film. Unpolarized (a) and cross-polarized (b) bright-field images. (c) Atomic force microscopy (AFM) height image of the blend film reveals embedded lamellar ribbons in the ring banding region. (d,e) The averaged Raman spectrum over the imaged region is fitted with multiple Gaussian peaks plotted in red and green for protonated- and deuterated-PE, respectively. (f–o) Raman images constructed with the peak heights of several representative Raman frequencies as specified. The pair in each column presents H-LLDPE (red) and D-HDPE (green) at an equivalent mode. The displayed intensity range of each image is set from zero to the maximum value. The white arrow indicates excitation polarization direction. The average powers are 10 and 15 mW for the continuum and narrowband pulses, and the CCD exposure time is 30 ms per pixel. The pixel spacing was set to be 200 nm, and the spatial resolution was 400 nm laterally.

in concentric ring banding (Figure 1b), which can be easily observed in cross-polarized bright-field images.[5,6] However, a lack of chemical contrast of the conventional methods makes it extremely challenging to address critical issues in a blend system. Specific unknowns are (a) whether two different molar mass or architecture chains cocrystallize in the same lamella; (b) where the crystalline and amorphous portions of the two species are located; (c) whether the degree of chain orientation is different between the two species; and (d) whether the above measurements can be quantitatively described. Here, we address these questions with collective and quantitative analyses of broadband coherent anti-Stokes Raman scattering (CARS) images observed with appropriate polarization control.

Broadband CARS microscopy, a 3-D chemical imaging modality with a high efficiency, has been developed to acquire simultaneous compositional and orientational images of multicomponent biological and materials systems.[7,8] Our current efforts are focused on demonstrating that the broadband CARS method can address key issues critical for performance of PE products, such as polymer chain diffusion and orientation immediately during and after the fusion (polymer welding) process and during mechanical failure. As the first step, we show in this work that this noninvasive and stain-free microscopy can provide new molecule-specific insights into the morphology of a semicrystalline blend. We investigate a 50:50 mass ratio PE blend that approximates the typical bimodal PE systems under commercial development for potable water and natural gas pipes, where long service life is critical. Deuterated medium molecular weight (MW) high density PE (D-HDPE) was used in the blend to provide image contrast from the protonated short-chain branched high MW linear low-density PE (H-LLDPE). Most of the Raman peaks of both deuterated- and protonated-PE have previously been well studied.[9−12] Among them, we use the peaks of CH_2 and CD_2 stretching modes and those of C−C stretching modes for quantitative image analysis of the two chain species herein.

Previously, researchers have used micro-Raman imaging to acquire both chemical and morphological information on heterogeneous polymer blends[13] and more recently on protonated-/deuterated-PE blends.[14] Due to an inherently weak signal from spontaneous Raman, however, they did not provide quantitative information on chemical identification and chain orientation with submicrometer spatial resolution, which is critical to the understanding of key microstructural factors.

dx.doi.org/10.1021/mz300546e | ACS Macro Lett. 2012, 1, 1347−1351

Recently, coherent Raman methods have been used to image heterogeneous polymer mixture samples at high speed by measuring strong multiphoton-enhanced signals at a specific Raman frequency.[15,16] In contrast to these prevailing single-frequency approaches, the *broadband* CARS imaging can simultaneously measure well-separated peaks in the fingerprint and C−H regions.[7,17] Here we demonstrate that broadband CARS microscopy reveals the difference in the distribution of the two different MW and architecture PE chains on three different physical dimensions.

Figure 1 shows bright field and atomic force microscopy (AFM) images of banded spherulites of the semicrystalline blend of H-LLDPE and D-HDPE prepared by slow cooling of a solution-blended sample from the melt at 170 °C. A Raman spectrum of the polymer blend, shown in Figure 1d,e, reveals more than 20 Raman peaks from either H-LLDPE or D-HDPE. The peak assignment is reconfirmed with independently measured Raman spectra from the homopolymers [Figure S1 in the Supporting Information (SI)] and compared with reported values.[9−12] Figure 1f-o shows CARS images constructed with several strong, characteristic Raman peaks, where the red and green colors represent H-LLDPE and D-HDPE respectively. The distinctively different Raman images constructed from a *single* acquisition reflect the complementary characteristics of the various Raman modes with different symmetries. A collective analysis of these images will enable us to determine both the local molecular orientation and spatial compositional variation. For example, the images of the CH_2 and CD_2 symmetrical stretching modes (Figure 1i,n) are almost opposite in their intensities to those of their corresponding C−C symmetrical stretching mode (Figure 1f,k), both of which are different from the images of the CH_2 and CD_2 bending modes (Figure 1h,m). The complementary characteristics of different modes allow one to separate the Raman contributions between composition variation and orientation variation.

To visualize the two different PE chains, we code the Raman intensity of H-LLDPE and D-HDPE in red and green, respectively, and combine the two images into one composite image on an equal intensity scale. In the composite image, a yellow color indicates that H-LLDPE and D-HDPE exist in an equal amount, and red or green indicate H-LLDPE or D-HDPE exists in excess, respectively. Figure 2a,b shows composite images of CARS intensities of CH_2 and CD_2 stretching modes acquired by linearly polarized excitation. Unlike the Maltese cross pattern in the cross-polarized bright-field image of Figure 1b, the CARS image shows bow-tie patterns, where the bright regions with strong CARS signals are parallel to the excitation polarization axis. The Raman intensity inside the bright quadrants changes only slightly along the radial direction, while inside the dark quadrant regions concentric undulations in Raman intensity are apparent. The undulation period in this CARS image is similar to that of the cross-polarized bright-field image of Figure 1b. The CARS image in Figure 2b is acquired after the polarization is rotated by 90° without changing the sampled area. It is clear that the bow-tie pattern is rotated by 90°, while the undulation characteristics remain unchanged, i.e., no radial variation in the bright regions and concentric undulation in the dark regions. This polarization dependence indicates that the crystal lamellae are distributed centro-symmetrically inside a spherulite. This symmetry of the ring banding is reconfirmed by the CARS image acquired by circularly polarized excitation (Figure 2c). In addition, the absence of undulations in the bright quadrant regions suggests

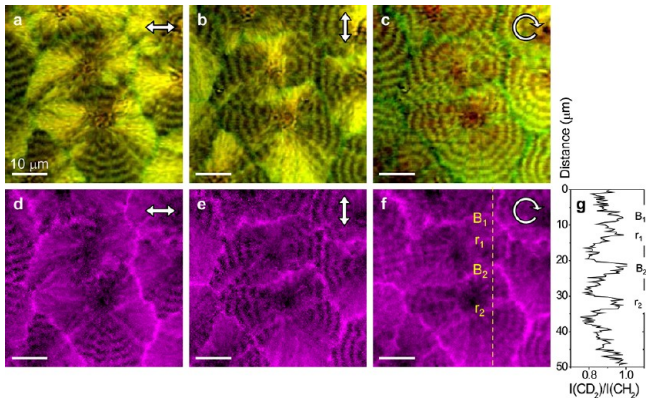

Figure 2. Polarization-dependent CARS images. (a−c) Composite images of CARS intensities of the CH_2 (2842 cm^{-1}, red) and CD_2 (2104 cm^{-1}, green) modes acquired at linearly and circularly polarized excitations. (d−f) Images of the ratio, $I(CD_2)/I(CH_2)$, calculated from the above intensity images. (g) A line profile of the dotted line indicated in (f), where the *B*'s correspond to spherulite boundaries and the *r*'s correspond to regions inside spherulites along bright radial lines, both of which convey CD_2 enrichment.

that the projection of CD and CH bonds along the radial direction does not change significantly across the ring bandings. This nearly constant Raman intensity in the bright region is consistent with the AFM measurement, where the relative sample thickness variation across a ring banding period is as low as 5% (Figure S2, Supporting Information). Therefore, the intensity undulation along the radial direction in the dark regions is mostly due to changes in molecular orientation, which is consistent with the existing collective twisting lamellae model,[18] such that the CD_2 and CH_2 bonds are going out-of-plane periodically. All of these results are consistent with established models of PE spherulites as depicted in Figure 3. What is not obvious from these established models is discussed below with our CARS results.

With CARS microscopy, we can image the distribution of the two species of chains inside and across spherulites. Most of the area of the spherulites appears to be yellow except some red in the central parts and green at the spherulitic boundaries,

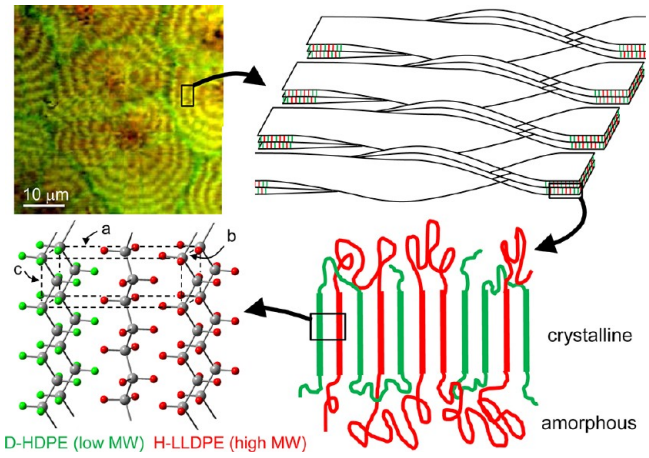

Figure 3. Schematic hierarchy of microscopic structure of PE blend spherulites consisting of semicrystalline lamellar ribbons. Green in the composite image indicates D-HDPE, and red indicates H-LLDPE. The dotted rectangular box in the molecular structure indicates the unit cell of crystalline PE, with the unit cell parameters (a, b, c) as indicated.

dx.doi.org/10.1021/mz300546e | *ACS Macro Lett.* 2012, 1, 1347−1351

suggesting that the high and low MW chains are in general well mixed with each other and that there exist more high MW chains at the center and more low MW chains at the boundary. The enrichment of D-HDPE at the boundaries of spherulites appears more clearly in the $I(CD_2)/I(CH_2)$ maps as shown in Figure 2d–f. The appearance of the spherulite boundaries appears to be similar in these three images of $I(CD_2)/I(CH_2)$ acquired at three different polarization conditions (Figure 2d–f). The similarity indicates that the excluded low MW chains are in an amorphous state with no preferred orientation. In Figure 2a–c, the red at the central regions of the spherulites indicates greater abundance of the high MW chains, and this phenomenon is also evident in the CD_2/CH_2 images (Figure 2d,e). The above observations indicate that the high MW, branched species initiate the nucleation process followed by the cocrystallization of both species in the growth of spherulites and expulsion of some of the noncrystallizing D-HDPE to boundaries. Keith and Padden studied phase segregation in spherulitic crystallization indirectly by observing changes in crystalline morphology when low MW or noncrystallizable molecules were added.[19] In this work, we directly observe the fractional enrichment of D-HDPE at the spherulite boundary and radial branching regions via chemical imaging. Lamellar stacks continuously grow in the radial direction and twist coherently with the neighboring stacks as evident from the banding; however, the intimacy of the seam among the neighboring stacks remains largely unknown. As the stacks grow, current models show the low MW species are expelled continuously at the growth front and eventually accumulate at the spherulite boundaries. What is less understood is the amount of the expelled species accumulating between stacks due to a lack of direct measurements. Analysis of CARS images in the tangential direction of the banding provides the structural information between adjacent branches. Figure 2g clearly shows that the D-HDPE enrichment occurs not only at the spherulite boundaries (B_1 and B_2) but also along some radial lines (r_1 and r_2). In Figure 2g, the magnitude of D-HDPE enrichments along the radial direction is almost as intense as at spherulite boundaries. Expelling of low MW D-HDPE into the interstack amorphous regions[20] along the side of growing radial branches is the likely cause of these radial D-HDPE enriched lines. This new ability to quantify microscopic phase separation and the local crystallinity is made possible only by having information on both chemical identification and molecular orientation.

In the line profiles of the C–C symmetrical stretching modes (Figure 4c), the amplitude of the D-HDPE undulations appears to be larger than that of the H-LLDPE undulations. For example, the C–C signal of D-HDPE fluctuates up to 52% of its peak value and that of H-LLDPE up to 47%. The undulation amplitude in a CARS image reflects the degree of coherence in cooperative lamellar twisting. This implies higher crystallinity in D-HDPE than H-LLDPE, since it is the crystalline portion that is aligned and twists in and out of the polarization direction, whereas the amorphous portion has no intrinsic orientation. A simple way to think of this is that if the sample were 100% crystalline, then the minimum of the intensity undulations would go to zero when the coherent C–C orientation from the crystal was perpendicular to the polarization direction; similarly, if the sample were 100% amorphous, there would be no change in intensity, i.e., no undulations. This greater molecular orientation of D-HDPE can be reconfirmed through another set of CARS measurements invoking the intensity ratio under

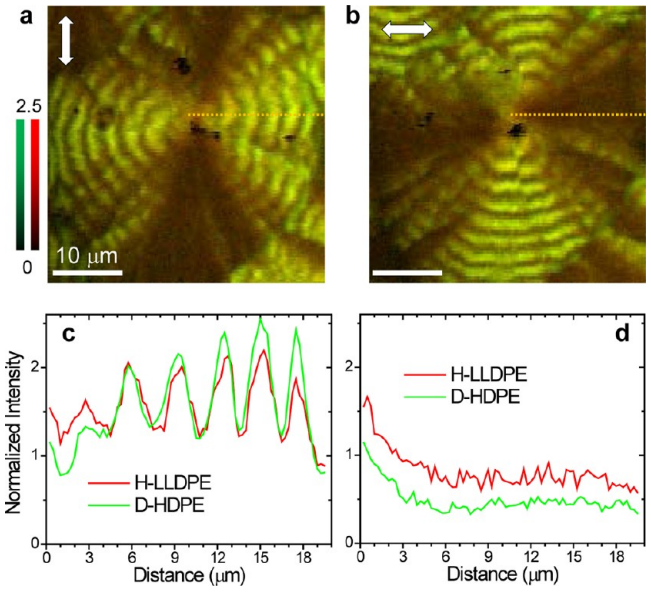

Figure 4. Raman intensity images and line profiles of the C–C stretching modes. The C–C symmetrical stretching Raman peaks at 1127 cm^{-1} (red) and 1146 cm^{-1} (green) for H-LLDPE and D-HDPE, respectively, are acquired back-to-back by two orthogonal linear polarizations. The Raman intensities are normalized by the image mean values and adjusted by the molar ratio (16:14) of the CH_2 and CD_2 blend with a mass ratio of 1:1. The line profiles of c,d are measured from the composite images of a,b, respectively.

two orthogonal polarization excitations. The maximum CARS intensity ratios of the line profiles in Figure 3c,d are 83% and 65% for D-HDPE and H-LLDPE, respectively. Line profiles from the CARS images of the CH_2/CD_2 stretching modes also exhibit similar results, which are discussed in the Supporting Information. These observations of molecular orientation difference are consistent with differential scanning calorimetry estimates of the crystalline mass fraction of slowly cooled samples of each component and of the blend (Figure S5, Supporting Information); more specifically, the estimates of crystallinity are ≈43% and ≈58% for H-LLDPE and D-HDPE, respectively. The lower crystallinity of H-LLDPE is expected due to the presence of hexyl side chains in this material.[21]

In conclusion, we have demonstrated that broadband CARS microscopy can simultaneously image chemical composition and molecular orientation of the high MW and the medium MW chains in a polyethylene semicrystalline blend. The new results lead to new findings: gradual exclusion of the medium MW chains from the spherulite center and its amorphous characteristics; higher degree of crystallinity of the medium MW chains in the ring banding; and filling of interstack amorphous regions by medium MW chains. The unique chemical imaging capability of broadband CARS microscopy can be used to investigate microscopic chemical structures of other types of multicomponent polymer blends. These new findings will be useful to study the structural and chemical changes as a function of mechanical stress and temperature, which will be more directly useful to understand the mechanical failure mechanisms.

■ EXPERIMENTAL SECTION

Sample preparation: The polyethylene samples studied were (a) the high molar mass component of a bimodal commercial PE pipe resin blend, a protonated linear low-density polyethylene (H-LLDPE) with

dx.doi.org/10.1021/mz300546e | ACS Macro Lett. 2012, 1, 1347–1351

a melt flow index (I21) of ≈0.3 g/10 min and 5 to 7 hexyl branches per 1000 CH_2 units, and (b) a perdeuterated high-density polyethylene (D-HDPE)—a medium molecular weight ($M_w \approx 2.9 \times 10^5$, $M_n \approx 1.07 \times 10^5$), with negligible branching. A mixture of D-HDPE and H-LLDPE at equal mass ratio was dissolved in *ortho*-dichlorobenzene at 160 °C under dry nitrogen for 45 min with vigorous stirring; the solid to liquid mass ratio was 2%. The hot solution was poured into a large reservoir of methanol at ice temperature, also under vigorous stirring, to precipitate the entire dissolved polymer instantaneously. The precipitate was collected via filtration followed by drying in a vacuum oven at 60 °C for 24 h. The samples in this work were prepared by melting the precipitate on a glass coverslip at 170 °C for ≈30 min and then slowly cooling to room temperature over 24 h; all the above thermal processing was carried out in an argon environment.

■ ASSOCIATED CONTENT

Supporting Information

Detailed description of measurement methods (CARS, AFM, and DSC). Further discussion on Figures 1, 2, and 4. This material is available free of charge via the Internet at http://pubs.acs.org.

■ AUTHOR INFORMATION

Corresponding Author

*E-mail: yjlee@nist.gov; wen-li.wu@nist.gov.

Notes

The authors declare no competing financial interest.

■ ACKNOWLEDGMENTS

The authors thank the Dow Chemical Company for providing the protonated H-LLDPE.

■ REFERENCES

(1) Aging Water infrastructure research Program. *Addressing the Challenge through Innovation*; Environmental Protection Agency: Cincinnati, OH, 2007; EPA/600/F−07/015.
(2) Samuels, R. J. *Structured Polymer Properties: Identification, Interpretation and Application of Crystalline Polymer Structure*; John Wiley & Sons Inc.: New York, 1974.
(3) Kakudo, M. *X-ray diffraction by polymers*; Elsevier: New York, 1972.
(4) Khoury, F.; Passaglia, E. In *Treatise on Solid State Chemistry*; Hannay, N., Ed.; Plenum: New York, 1976; Vol. 3.
(5) Keller, A. *J. Polym. Sci.* **1955**, *17*, 351−364.
(6) Lotz, B.; Cheng, S. Z. D. *Polymer* **2005**, *46*, 577−610.
(7) Kee, T. W.; Cicerone, M. T. *Opt. Lett.* **2004**, *29*, 2701−2703.
(8) Lee, Y. J.; Moon, D.; Migler, K. B.; Cicerone, M. T. *Anal. Chem.* **2011**, *83*, 2733−2739.
(9) Bower, D. I.; Maddams, W. F. *The Vibrational Spectroscopy of Polymers*; Cambridge Solid State Science Series; Cambridge University Press: New York, 1989.
(10) Liao, Z.; Pemberton, J. E. *J. Phys. Chem. A* **2006**, *110*, 13744−13753.
(11) Tasumi, M.; Shimanouchi, T. *J. Chem. Phys.* **1965**, *43*, 1245−1258.
(12) Masetti, G.; Abbate, S.; Gussoni, M.; Zerbi, G. *J. Chem. Phys.* **1980**, *73*, 4671−4679.
(13) Tanaka, H.; Ikeda, T.; Nishi, T. *Appl. Phys. Lett.* **1986**, *48*, 393−395.
(14) Morgan, R. L.; Hill, M. J.; Barham, P. J.; Van der Pol, A.; Kip, B. J.; Ottjes, R.; Van Ruiten, J. *Polymer* **2001**, *42*, 2121−2135.
(15) Zumbusch, A.; Holtom, G. R.; Xie, X. S. *Phys. Rev. Lett.* **1999**, *82*, 4142−4145.
(16) Freudiger, C. W.; Min, W.; Saar, B. G.; Lu, S.; Holtom, G. R.; He, C.; Tsai, J. C.; Kang, J. X.; Xie, X. S. *Science* **2008**, *322*, 1857−1861.
(17) von Vacano, B.; Meyer, L.; Motzkus, M. *J. Raman Spectrosc.* **2007**, *38*, 916−926.
(18) Keith, H. D.; Padden, F. J. *Macromolecules* **1996**, *29*, 7776−7786.
(19) Keith, H. D.; Padden, F. J. *J. Appl. Phys.* **1964**, *35*, 1270−1285.
(20) Cagiao, M. E.; Calleja, F. J. B.; Vanderdonckt, C.; Zachmann, H. G. *Polymer* **1993**, *34*, 2024−2029.
(21) Flory, P. J. *Trans. Faraday Soc.* **1955**, *51*, 848−857.